Temperature-dependent perpendicular anisotropy and Gilbert damping of $L1_0$-FePd films: Role of noble-metal buffer layers

Dingbin Huang [1,2] Deyuan Lyu [3] Xinjun Wang,[4] Michael B. Katz,[5] Delin Zhang,[3] Jian-Ping Wang [3] Daniel B. Gopman [5] and Xiaojia Wang [1,2,*]

[1]*Department of Mechanical Engineering, University of Minnesota, Minneapolis, Minnesota 55455, USA*
[2]*Minnesota Institute for Ultrafast Science, University of Minnesota, Minneapolis, Minnesota 55455, USA*
[3]*Department of Electrical and Computer Engineering, University of Minnesota, Minneapolis, Minnesota 55455, USA*
[4]*Department of Materials Science and Engineering, University of Maryland, College Park, Maryland 20742, USA*
[5]*Materials Science and Engineering Division, National Institute of Standards and Technology, Gaithersburg, Maryland 20899, USA*

(Received 2 May 2022; revised 11 May 2022; accepted 1 November 2022; published 23 November 2022)

The moderate bulk perpendicular magnetic anisotropy (PMA, $K_u \approx 1\,\mathrm{MJ/m^3}$) and low Gilbert damping ($\alpha < 0.01$) make $L1_0$-FePd a promising candidate for energy-efficient and nonvolatile spintronic devices with large areal densities (down to 5-nm pitch sizes or even lower). Existing applications subject spintronic devices to a wide range of operating temperatures (e.g., −55 to 150 °C). To better address the technological viability of FePd for spintronic applications, it is of utmost importance to evaluate the material performance of $L1_0$-FePd (e.g., anisotropy strength and Gilbert damping) at elevated temperatures. In this work, we systematically investigate the effect of buffer layers (Cr/Pt, Cr/Ru, Cr/Rh, Cr/Ir, and Ir) on the PMA and Gilbert damping of $L1_0$-FePd from room temperature (RT, 25 °C) to 150 °C using the time-resolved magneto-optical Kerr effect metrology. It is found that the effective anisotropy field ($H_{k,eff}$) of FePd decreases with the testing temperature (T_{test}) and the ratio of $H_{k,eff}$(150 °C)/$H_{k,eff}$(25 °C) is positively correlated to the degree of $L1_0$ phase ordering. The Gilbert damping of $L1_0$-FePd either increases with T_{test} or stays nearly constant over the T_{test} range. We attribute the temperature dependence of Gilbert damping to the spin diffusion length of the metallic buffer layer (λ), presumably through the spin pumping effect. Results of this work provide guidance to tailor $L1_0$-FePd properties through buffer layer engineering for applications in spintronic devices over wide operating temperature ranges.

DOI: 10.1103/PhysRevMaterials.6.113402

I. INTRODUCTION

As conventional semiconductor devices confront a scaling limit and a lack of nonvolatility, nanomagnet-based spintronic devices have been proposed as next-generation memory and logic systems [1]. For example, spin-transfer torque magnetoresistive random access memory (STT-MRAM), both nonvolatile and highly scalable, has attracted extensive interest from research and industrial communities. The speed and energy efficiency of spintronic devices are dictated by the dynamical motion of a nanomagnet's magnetization (**M**), described by the Landau-Lifshitz-Gilbert (LLG) equation $d\mathbf{M}/dt = -|\gamma|\mathbf{M} \times \mathbf{H_{eff}} + \alpha/M_s(\mathbf{M} \times d\mathbf{M}/dt)$ [2]. The first term describes magnetization precession about its effective field, with γ and $\mathbf{H_{eff}}$ being, respectively, the gyromagnetic ratio and effective field. The second term is a phenomenological term that accounts for the dissipation of magnetic energy, where α is the Gilbert damping describing how fast the magnetization precession damps towards the equilibrium direction and M_s is saturation magnetization. For STT-MRAM, materials with a high perpendicular magnetic anisotropy (PMA, K_u) and a low α are essential to simultaneously realize device miniaturization, high thermal stability, and low energy consumption.

Given its large crystalline magnetic anisotropy ($K_u \approx 1\,\mathrm{MJ/m^3}$) and low Gilbert damping ($\alpha < 0.01$), $L1_0$-FePd has been proposed as a promising candidate for spintronic applications. To synthesize $L1_0$-FePd films with desired properties (high K_u and low α), considerable efforts have been devoted to optimizing the growth conditions [3–7] and structure design [5,7–11] of FePd stacks. FePd films with high K_u and low Gilbert damping at room temperature (RT) have been achieved via buffer layer engineering [9]. To date, most literature studies on $L1_0$-FePd focused on RT properties [7,9,12] and reports on high-temperature properties are limited [10]. Considering the MRAM operating temperature range (−55 to 150 °C) [13], the temperature-dependent PMA and Gilbert damping of $L1_0$-FePd are crucial for the MRAM device performance.

Owing to the thermal fluctuation of magnetic moments, the anisotropy energy (K_u) scales with magnetization, which is temperature dependent. In addition, K_u was also shown to correlate with the $L1_0$-phase ordering parameter (S) of FePd with varying buffer layers at RT [9]. Thus, buffer layer engineering provides a possible way to tailor the T dependence of PMA for $L1_0$-FePd. As for the Gilbert damping, both intrinsic damping (resulting from the spin-orbital coupling dominant in metallic systems) and spin pumping can contribute [14,15].

*Corresponding author: wang4940@umn.edu

TABLE I. A summary of sample stack information (layer thicknesses are given in nm in parentheses), $L1_0$-phase ordering parameter [9], and RT saturation magnetization (M_s).

Sample no.	Stack	S	RT M_s (kA/m)
1	MgO (001) sub./FePd(8)/Ru(2)/Ta(3)	0.55 ± 0.06	1160 ± 145
2	MgO (001) sub./Cr(15)/Pt(4)/FePd(8)/Ru(2)/Ta(3)	0.82 ± 0.02	930 ± 116
3	MgO (001) sub./Cr(15)/Ru(4)/FePd(8)/Ru(2)/Ta(3)	0.64 ± 0.05	882 ± 110
4	MgO (001) sub./Cr(15)/Rh(4)/FePd(8)/Ru(2)/Ta(3)	0.47 ± 0.02	753 ± 94
5	MgO (001) sub./Cr(15)/Ir(4)/FePd(8)/Ru(2)/Ta(3)	0.68 ± 0.03	1182 ± 148
6	MgO (001) sub./Ir(11)/FePd(8)/Ru(2)/Ta(3)	0.54 ± 0.05	1035 ± 129
7	MgO (001) sub./Cr(15)/Pt(4)/FePd(12)/Ru(2)/Ta(3)	0.71 ± 0.09	1015 ± 127
8	MgO (001) sub./Cr(15)/Pt(4)/FePd(16)/Ru(2)/Ta(3)	0.67 ± 0.02	840 ± 105

The intrinsic damping of $L1_0$-$FePd_{1-x}Pt_x$ ternary alloy has been well captured by the torque-correlation model, considering contributions from the interband (increases with T) and intraband (decreases with T) electronic transitions [16–20]. The combined effect results in the minimum of intrinsic damping around RT for $L1_0$-FePd, where the temperature dependence is weak [21]. For the spin-pumping effect, spin currents driven by magnetization dynamics can be injected from a magnetic layer to its adjacent layers, which increases damping. Hence, the choice of buffer layers (as adjacent underlayers to FePd) can be used to tune the Gilbert damping of $L1_0$-FePd [22]. However, the temperature dependence of Gilbert damping due to spin pumping was rarely reported previously [23], not to mention the impact of buffer layers on the Gilbert damping at elevated temperatures.

In this work, we systematically investigate the effects of noble-metal buffer layers (including Cr/Pt, Cr/Ru, Cr/Rh, Cr/Ir, and Ir) on the temperature-dependent magnetic anisotropy and Gilbert damping of $L1_0$-FePd films. We perform time-resolved magneto-optical Kerr effect (TR-MOKE) measurements to extract both the effective anisotropy field ($H_{k,eff}$) and α of $L1_0$-FePd from RT (25 °C) to 150 °C. The dependence of $H_{k,eff}$ on temperature is correlated to the $L1_0$-phase ordering parameter of FePd manipulated by buffer layer engineering. The temperature-dependent α of $L1_0$-FePd is explored and attributed to the spin diffusion lengths of buffer layers, which lead to the different enhancement for the Gilbert damping via the spin-pumping effect.

II. SAMPLE FABRICATION AND EXPERIMENTAL METHODS

Eight FePd samples in total are studied in this work. All FePd films were grown on MgO(001) substrates and capped with Ru(2)/Ta(3) layers (numbers in parentheses are thicknesses in nm). Sample 1 was grown on bare MgO, serving as a reference baseline. Samples 2–8 have different buffer layers, including Cr/Pt, Cr/Ru, Cr/Rh, Cr/Ir, and Ir. All samples were prepared by ultrahigh vacuum dc magnetron sputtering. For each sample, the $L1_0$-phase ordering parameter (S) was calculated based on x-ray diffraction (XRD) [9]. The layer stacking structures, ordering parameters, and saturation magnetizations of all sample are summarized in Table I. Scanning transmission electron microscopy (STEM) and vibrating sample magnetometry (VSM) measurements were conducted to obtain structural information and hysteresis (M-H) loops, respectively. Details regarding sample fabrication and characterization can be found in Sec. S1 of the Supplemental Material (SM) [24]. The magnetization dynamics was captured with TR-MOKE, allowing for the determination of $H_{k,eff}$ and α [10,25,26].

III. RESULTS AND DISCUSSION

Figures 1(a) and 1(b) show a representative high-angle annular-dark-field (HAADF) STEM image of sample 6, which indicates the cube-on-cube growth proceeding from the MgO(001) substrate through the Ir(001) buffer and the FePd(001) layer with the polycrystalline Ru/Ta capping layers grown as a protective capping complex. The STEM image also reveals the smooth interface between Ir and FePd and $L1_0$ ordering. Based on the STEM image, the average in-plane (a) and out-of-plane lattice parameters (c) are calculated. For Ir, $a = c = 0.384$ nm, matching the value obtained from XRD (0.384 nm) [27]. For FePd, $a = 0.387$ nm and $c = 0.375$ nm, close to the lattice parameters previously reported for $L1_0$-FePd ($a = 0.385$ nm and $c = 0.373$ nm) [28,29].

To obtain the temperature-dependent magnetic properties, VSM measurements were conducted as a function of the testing temperature (T_{test}) from RT to 125 °C with a step of 25 °C. Owing to instrument limitations, VSM measurements were not performed at 150 °C. Figures 1(c) and 1(d) show the representative hysteresis loops of sample 2 measured at RT and 125 °C, respectively. Hysteresis loops of all samples can be found in Sec. S1 of the SM [24]. From VSM measurements, apparent perpendicular magnetic anisotropy and saturation magnetization can be identified for all samples at various temperatures. The temperature dependence of normalized magnetization $M_s(T)/M_s(25\,°C)$ is depicted in Fig. 1(e). For all samples, the decrease in M_s is within 10% over the T_{test} range. Figure 1(f) shows the ratio of $M_s(T)/M_s(25\,°C)$ as a function of S. A positive correlation is observed between the normalized M_s and T_{test}, suggesting that magnetization decreases faster for samples with a lower S within the T_{test} range. This result is consistent with the work by Okamoto *et al.* on $L1_0$-FePt, where the magnetization ratio $M_s(T)/M_s(10\,K)$ dropped faster for lower-ordering samples [30].

TR-MOKE measurements were performed on all samples from RT to 150 °C, with an interval of 25 °C to extract temperature-dependent $H_{k,eff}$ and α. Figure 2(a) shows the schematics of TR-MOKE measurement configuration on a sample stack, in which ultrafast pump and probe pulses are

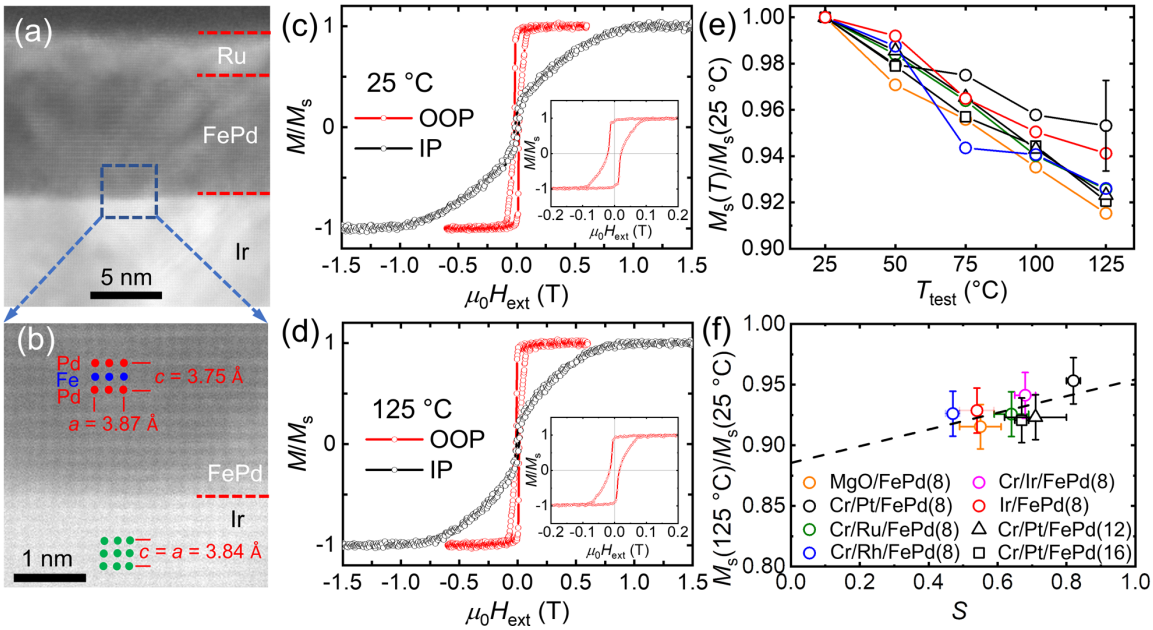

FIG. 1. (a) A HAADF STEM image of MgO/Ir(11)/FePd(8) sample. (b) A magnified Fig. 1(a) around the Ir/FePd interface. (c),(d) Hysteresis loops of Cr/Pt/FePd(8) sample at (c) 25 °C (RT) and (d) 125 °C. The insets show the out-of-plane M-H loops near $H_{ext} = 0$. (e) Magnetization ratio $M_s(T)/M_s(25\,°C)$ as a function of T_{test} from RT to 125 °C, for all samples. For better visualization, one representative error bar is shown given that all data points (except for data at 25 °C, which do not have uncertainties) have similar error bars (∼±2%). (f) Magnetization ratio $M_s(125\,°C)/M_s(25\,°C)$ vs S. The dashed line shows the linear fitting. (e),(f) share the same figure legends.

focused onto the sample surface to excite and detect magnetization precession. Figure 2(b) illustrates the magnetization precession signals measured on sample 2 at RT under varying external magnetic fields (H_{ext}). For better visualization, in Fig. 2(b), the signals of individual scans are normalized to their largest variations (i.e., the difference between the highest and lowest values of the signal for each scan) and offset by an arbitrary number. For our measurement configuration ($70° < \theta_H < 90°$), the actual amplitude of TR-MOKE signals changes with H_{ext} and has the highest value when $H_{ext} \approx H_{k,eff}$ [31]. The precession frequency (f) and relaxation time (τ), which are obtained via fitting TR-MOKE signals, will be used for determining $H_{k,eff}$ and α [10,26]. Figures 2(c) and 2(d) illustrate the field-dependent f and $1/\tau$ of sample 2 at RT and corresponding fitting curves to extract $H_{k,eff}$ and α (see Sec. S2 of the SM for fitting methods and data processing for all samples [24]). To eliminate extrinsic contributions to the extracted α, only high-field data ($H_{ext} >\sim 2H_{k,eff}$) in the $1/\tau$ vs H_{ext} plot are used for fitting α. In Fig. 2(d), the experimental data deviate from the model noticeably at low fields ($H_{ext} < 11$ kOe), likely due to the low-field loss [32].

Figure 3(a) shows the temperature-dependent $H_{k,eff}$ of all samples measured from RT (25 °C) to 150 °C. Additional measurements were taken after quenching samples back to RT. The RT measurements before and after heating give consistent results (within 3% of each other), justifying the exclusion of possible irreversible effects (e.g., oxidation and atom diffusion) during TR-MOKE measurements. The anisotropy energy of $L1_0$-FePd is scaled down with magnetization following the Callen-Callen power law

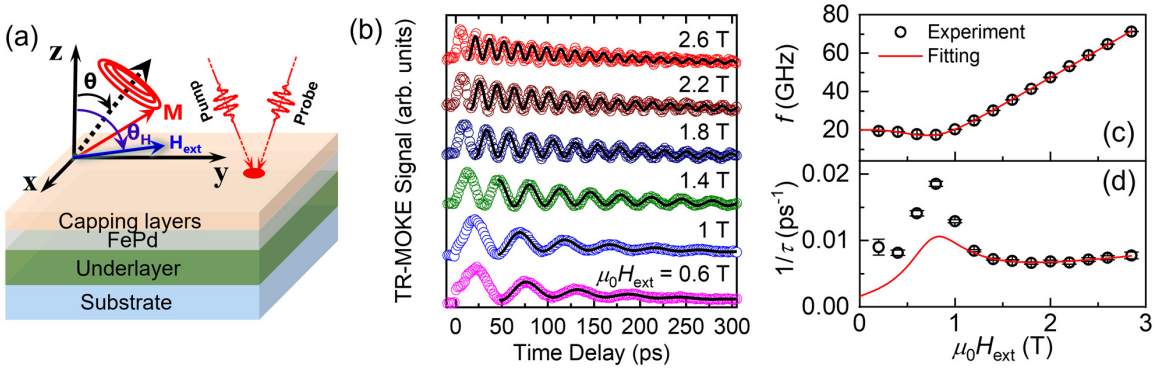

FIG. 2. (a) The schematics of sample stack and TR-MOKE measurement configurations ($\theta_H \approx 80°$). (b) TR-MOKE signals (symbols) measured on Cr/Pt/FePd(8) under varying H_{ext} at RT and their fitting curves (solid lines). (c),(d) An example of fitting f vs H_{ext} and $1/\tau$ vs H_{ext} to extract $H_{k,eff}$ and α from Cr/Pt/FePd(8). Circles and curves represent experimental data and modeling fitting, respectively.

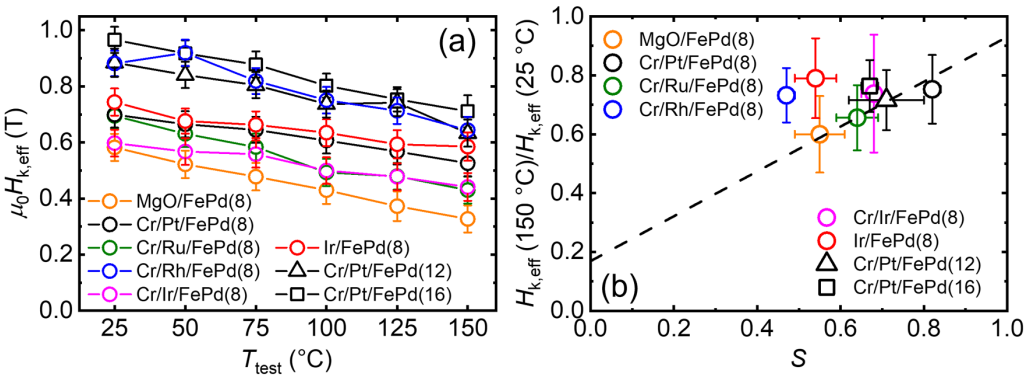

FIG. 3. (a) $H_{k,eff}$ vs T_{test} for all FePd films deposited on different buffer layers. (b) The ratio of $H_{k,eff}$ at 150 °C to its RT value as a function of S. The dashed line guides the general trend.

via $K_u(T)/K_u(0\,K) = [M_s(T)/M_s(0\,K)]^n$ (with n being reported as 2–4) [33–37]. Therefore, the effective anisotropy field ($H_{k,eff} = 2K_u/M_s - 4\pi M_s$) also decreases with T. As expected, a general decreasing trend of $H_{k,eff}$ on temperature is observed for all samples from Fig. 3(a). However, the robustness of $H_{k,eff}$ (i.e., the remaining percentage of $H_{k,eff}$ at high temperatures) differs from sample to sample.

Figure 3(b) summarizes the ratio of $H_{k,eff}(150\,°C)/H_{k,eff}(25\,°C)$ with respect to S for all samples. Similar to the normalized magnetization, a positive correlation is observed between the $H_{k,eff}$ ratio and S (guided by the black dashed line). It indicates that samples with a lower long-range ordering suffer a more significant reduction in the effective anisotropy field resulting from the thermal fluctuations of the magnetization and magnetic anisotropy. For Cr/Rh/FePd(8) and Ir/FePd(8), we note a more robust $H_{k,eff}$ at 150 °C than expected for the estimated ordering parameter S. We speculate this could be caused by the underestimation of S for these two samples resulting from the overlap between the (002) reflection peaks of Ir and Rh with that of (002) FePd, which tend to overestimate the (002) FePd intensity and thus reduces S. Based on $M_s(T)$ and $H_{k,eff}(T)$, $K_u(T)$ can be calculated, which follows the Callen-Callen power law: $K_u(T)/K_u(25\,°C) = [M_s(T)/M_s(25\,°C)]^n$ with $n = 2.89$ for samples in this work [Fig. S9(a) [24]]. The resulting values of $K_u(125\,°C)/K_u(25\,°C)$ also exhibit a positive correlation with S [Fig. S9(b)], further confirming that a high S is beneficial for maintaining thermal stability of FePd at elevated temperatures. Further details regarding $K_u(T)$ are provided in Sec. S3 of the SM [24].

The temperature-dependent α of five 8-nm FePd samples is plotted in Fig. 4(a). We could not extract α for sample 5 due to its weak precessional signals. From Fig. 4(a), α either increases (Cr/Ru/FePd and Cr/Pt/FePd) or stays nearly constant (MgO/FePd, Cr/Rh/FePd, and Ir/FePd) with T_{test}. The α values from TR-MOKE range between ∼0.005 and ∼0.015 for different samples. In general, noble-metal buffer layers can affect the Gilbert damping of FePd via the spin-pumping effect and the $L1_0$-phase ordering. As shown in Table I, the sample ordering parameters of this work range from ∼0.5 to 0.8. Within this range, the calculated intrinsic Gilbert damping only varies by ∼0.002 [21]. This relatively weaker dependence of intrinsic damping on S might not be deterministic, considering the more scattered experimental data of Gilbert damping in the literature, where α could easily spread ∼±0.002 around the trend line [7]. Thus, the much larger difference in RT α observed for our samples (∼0.01) requires a more detailed examination.

As the major difference among the samples lies in the buffer-layer materials, we then hypothesize that the spin-pumping effect between FePd and its buffer layer plays a more important role in affecting α for our samples. The spin-pumping enhanced Gilbert damping can be expressed as [38,39]

$$\alpha_{sp} = g\mu_B \frac{g_{\uparrow\downarrow}}{4\pi d M_s}(1 - e^{-2t/\lambda}), \tag{1}$$

where g and μ_B represent the g factor and Bohr magneton, respectively. $g_{\uparrow\downarrow}$ is the intrinsic spin-mixing conductance. The thicknesses of the ferromagnetic (FM) layer ($L1_0$-FePd) and the adjacent nonmagnetic (NM) layer (the buffer layer) are respectively denoted as d and t. M_s is the saturation magnetization of the FM layer and λ is the spin-diffusion length of the NM layer. The term $(1 - e^{-2t/\lambda})$ describes the impact of backflow spin currents. When λ is much smaller than t, the backflow term approaches 1 and $\Delta\alpha_{sp}$ saturates at $g\mu_B g_{\uparrow\downarrow}/4\pi d M_s$. Based on Eq. (1), buffer layer affects α_{sp} mainly through $g_{\uparrow\downarrow}$ and λ. When λ/t is small and $g_{\uparrow\downarrow}$ is high, spin-pumping enhancement on damping can be significant. The literature reported λ values of different buffer-layer materials are listed in Table II. At RT, Ru has the longest λ ($\lambda_{Ru} \approx 6$ nm) [40–42] compared with Pt ($\lambda_{Pt} < 2$ nm) [43], Ir ($\lambda_{Ir} = 1.3$ nm) [44], and Rh ($\lambda_{Rh} < 1$ nm) [45]. As for the baseline reference sample 1 [MgO/FePd(8)], the bare MgO

TABLE II. A summary of spin-diffusion length (λ) and the thickness (t) of NM buffer layers, and the estimated interfacial spin mixing conductance ($g_{\uparrow\downarrow}$) of the NM/FePd interface.

Interfaces	λ (nm)	t (nm)	$g_{\uparrow\downarrow}$ (nm^{-2})
Ir/FePd	1.3 [44]	11	27 ± 5
Rh/FePd	<1 [45]	4	50 ± 5
Pt/FePd	<2 [43]	4	29 ± 5
Ru/FePd	6 ± 2 [40–42]	4	7 ± 2 [53,54]

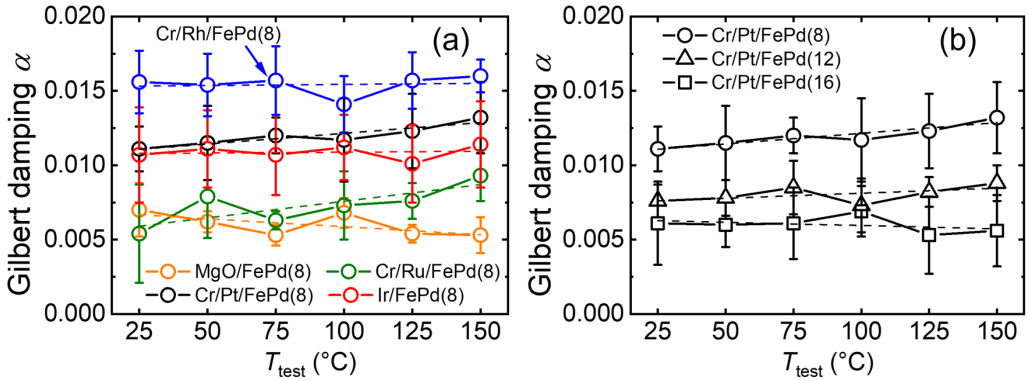

FIG. 4. Gilbert damping as a function of T_{test} for (a) 8-nm FePd samples and (b) Pt-seeded FePd samples. In panels (a) and (b), symbols represent experimental data and dashed lines are corresponding linear fittings that are used to calculate the change of α (denoted as $\Delta\alpha$) in Fig. 5.

substrate is a NM insulator, which quenches the spin-pumping effect. This qualitatively explains our observation of α: at RT, the values of α are the lowest for samples 1 and 3 [$\alpha = 0.007$ for MgO/FePd(8) and 0.0054 for Cr/Ru/FePd(8)]. The smaller α for the Cr/Ru-buffered film compared to FePd grown directly on MgO reflects additional subtleties that underlie damping measurements in FePd thin films, including a measurement uncertainty of ~0.002, variation in S between these two samples [21], and an empirically observed spread of α for a given S [7]. Additionally, for samples 2, 7, and 8 with a Pt buffer layer, α decreases from 0.016 to 0.006 at RT as the FePd thickness d increases from 8 to 16 nm [see Fig. 4(b)], also supporting the significant impact of spin pumping on α. It should be noted that as the FePd film grows, the desirable $L1_0(001)$ tends to nucleate near the Pt/FePd interface; while $L1_0(100)$ and $L1_0(010)$ could form in the regions away from the Pt/FePd interface [11]. Such growth features will introduce microstructural variations along the thickness direction. As a result, implementing a linear extrapolation of α vs $1/d$ (with d being the FePd film thickness for samples 2, 7, and 8) is unlikely to provide the intrinsic damping accurately, as typically has been done in the spin-pumping observations of other materials systems [39,46].

To separate the impacts of $g_{\uparrow\downarrow}$ and λ on α_{sp} for samples with different buffer layers, we estimate the values of $g_{\uparrow\downarrow}$ based on RT damping results. The smallest value of Gilbert damping measured from TR-MOKE ($\alpha_{min} = 0.0054$) is taken as the sum of the intrinsic damping contribution and any possible capping-layer contribution. This allows the spin-pumping enhanced α_{sp} to be calculated as $\alpha_{sp} = \alpha(25\,^{\circ}\mathrm{C}) - \alpha_{min}$ at RT. In the calculation of $g_{\uparrow\downarrow}$ based on Eq. (1), the NM layer thickness t is 4 nm for all samples except for sample 6 where $t = 11$ nm. The Cr layer is not considered since it has been demonstrated that a thick adjacent Cr layer ($t \geqslant 10$ nm) does not induce noticeable spin-pumping enhancement [47,48]. The calculated $g_{\uparrow\downarrow}$ values are summarized in Table II. The $g_{\uparrow\downarrow}$ values for Ir/FePd and Pt/FePd are comparable to those reported for Py/Ir ($g_{\uparrow\downarrow} = 25.2 \pm 0.5\,\mathrm{nm}^{-2}$) [49] and Py/Pt ($g_{\uparrow\downarrow} = 21 - 25.8\,\mathrm{nm}^{-2}$) [50–52]. To the best of our knowledge, there is no $g_{\uparrow\downarrow}$ value reported for an Rh/FM interface. As for Ru/FePd, we do not have enough sensitivity to estimate $g_{\uparrow\downarrow}$ since the difference between the measured damping and α_{min} is too small compared with the measurement uncertainty. Considering that $g_{\uparrow\downarrow}$ is insensitive to the FM properties for highly conductive FM layers [53], we use the effective $g_{\uparrow\downarrow}$ reported for Ru/FeCo with a backflow correction [54].

The temperature dependence of α can further support the spin-pumping effect as an important contributing factor to Gilbert damping. For sample 1 [MgO/FePd(8)] with no buffer layer, the temperature dependence of α is mainly determined by the intrinsic damping of the FePd layer and the spin-pumping enhancement possibly from the [Ru/Ta] capping layer. The overall effect of these two contributions leads to an α that is approximately independent of T_{test} within the T_{test} range. This suggests that any temperature dependence observed for other samples with buffer layers is mainly caused by the spin-pumping effect between FePd and its buffer layer. Since the spin-diffusion length roughly scales with the electron conductivity of metals, λ becomes shorter as temperature increases [40], and thus α_{sp} increases with temperature. It is worth noting that $g_{\uparrow\downarrow}$ and M_s are also temperature dependent. However, for the range of $T_{test} < 0.6T_C$, the impact of T_{test} on $g_{\uparrow\downarrow}/M_s$ is weak; therefore, we neglect the temperature dependence of $g_{\uparrow\downarrow}/M_s$ when calculating α_{sp} using Eq. (1) [55,56]. This leads to the temperature-dependent λ as the primary factor responsible for the change in α_{sp} at elevated temperatures.

For the three Pt-seeded samples with the same buffer layer but varying FePd thicknesses, the increase in α with T_{test} becomes smaller when the FePd thickness d increases, as shown in Fig. 4(b). This agrees with the spin-pumping explanation, in which, α_{sp} is inversely proportional to the thickness of the FM layer (d); thus, the temperature dependence of α due to the spin-pumping effect is averaged more over a thicker FePd film and becomes less apparent.

For samples with different buffer layer materials, the effect of spin pumping on the temperature-dependent α can be better visualized in Fig. 5(a), which plots $\Delta\alpha$ (change in α from RT to 150 °C) vs λ/t with λ being the spin-diffusion length at RT. Apparently, there exists a positive correlation between $\Delta\alpha$ and the normalized λ/t for 8-nm FePd samples with different

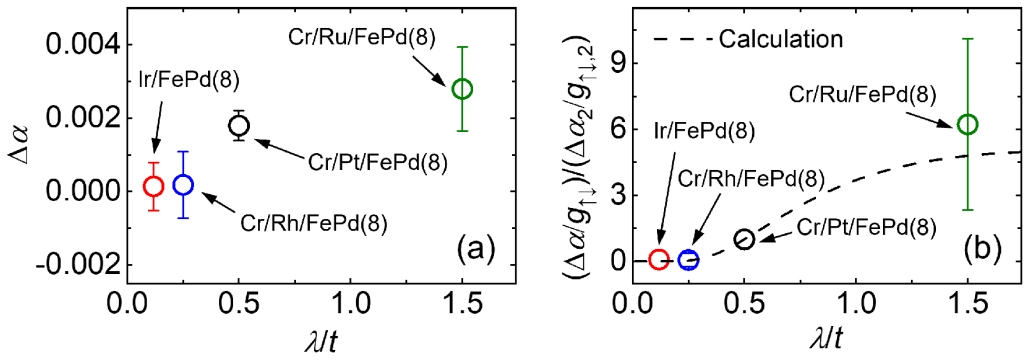

FIG. 5. (a) The change of α vs the spin-diffusion length λ normalized to the buffer-layer thickness t [$\Delta\alpha = \alpha(150\,^{\circ}\mathrm{C}) - \alpha(25\,^{\circ}\mathrm{C})$]. (b) Comparison of the theoretically predicted (dashed line) and experimentally measured (symbols) trend for $(\Delta\alpha/g_{\uparrow\downarrow})/(\Delta\alpha_2/g_{\uparrow\downarrow,2})$ vs λ/t.

buffer layers. The α of FePd is less temperature dependent when grown on a NM buffer layer with a smaller λ/t. Based on Eq. (1), as λ/t approaches 0, any further decrease in λ (as temperature increases) will not augment α_{sp} since the backflow of spin currents is already nearly fully suppressed.

The trend in Fig. 5(a) qualitatively agrees with the spin-pumping explanation. However, similar to the RT damping discussion, both $g_{\uparrow\downarrow}$ and λ can affect $\Delta\alpha$ as temperature increases. Thus, we perform an analysis of $\Delta\alpha$ by scaling λ with temperature as $\lambda = CT^{-m}$ (with m being a positive constant) [40,57] to separate contributions from $g_{\uparrow\downarrow}$ and λ. The change in damping due to temperature difference can then be calculated as

$$\Delta\alpha = \Delta\alpha_{sp} = \frac{\partial\alpha_{sp}}{\partial\lambda}\frac{d\lambda}{dT}\Delta T = g_{\uparrow\downarrow}\frac{g\mu_B}{4\pi d M_s}\exp(-2t/\lambda)\frac{2t}{\lambda}\frac{m\Delta T}{T}. \quad (2)$$

By dividing both sides with $g_{\uparrow\downarrow}$, the impact of $g_{\uparrow\downarrow}$ can be separated. The ratio of $\Delta\alpha/g_{\uparrow\downarrow}$ can be further normalized to the ratio of sample 2 [Cr/Pt/FePd(8)] to simplify the comparison by canceling out all prefactors:

$$(\Delta\alpha/g_{\uparrow\downarrow,i})/(\Delta\alpha_2/g_{\uparrow\downarrow,2}) = \left[\exp\left(-\frac{2t_i}{\lambda_i}\right)\frac{2t_i}{\lambda_i}\right]\Big/\left[\exp\left(-\frac{2t_2}{\lambda_2}\right)\frac{2t_2}{\lambda_2}\right], \quad (3)$$

where, the subscript "i" and "2" represent sample i (i = 2, 3, 4, 6) and sample 2, respectively. Here, we choose sample 2 as the normalization factor considering $g_{\uparrow\downarrow}$ for Pt/FM interfaces is well studied in the literature [53]. Figure 5(b) shows the dependence of $\Delta\alpha/g_{\uparrow\downarrow}$ on λ/t from both measurements and the theoretical calculation using Eq. (3). It is clear that the impacts of λ/t on normalized $\Delta\alpha/g_{\uparrow\downarrow}$ can be well captured by the model further supporting the spin-pumping explanation.

IV. CONCLUSION

We systematically study the effects of noble-metal layers on the temperature dependence of the effective anisotropy field and Gilbert damping of $L1_0$-FePd. The results show that FePd layers grown on Ir, Rh, and Pt can reserve a higher fraction of their RT $H_{k,eff}$ at 150 °C, compared with those grown on Ru and bare MgO. In general, the FePd film with a higher $L1_0$-phase ordering parameter has a lesser $H_{k,eff}$ change with increased temperature. The increase in the Gilbert damping at high temperature is more noticeable when the spin-diffusion length of the buffer layer is large. For FePd films grown on Rh or Ir with a spin-diffusion length shorter than the buffer-layer thickness, α is almost independent of temperature. The choice of the buffer-layer materials can affect the temperature dependence of α, presumably through the spin-pumping effect. The reduction in λ at high temperatures suppresses the spin currents flowing back to the FePd layer and thus enhances α. However, for FePd films with considerably larger thicknesses than the spin-diffusion length of the buffer layer, the backflow spin currents are sufficiently weak at RT, and a further decrease in λ at elevated temperatures will not lead to a noticeable enhancement of α.

ACKNOWLEDGMENTS

This work was primarily supported by the National Science Foundation (NSF, Grant No. CBET-2226579). The authors also gratefully acknowledge the partial support from the ERI program (FRANC) "Advanced MTJs for computation in and near random access memory" by DARPA, and ASCENT, one of six centers in JUMP (a Semiconductor Research Corporation program, sponsored by MARCO and DARPA), the National Institute of Standards and Technology, and the UMN MRSEC Seed Program (NSF, Grant No. DMR-2011401). D.B.H. would like to thank the support from the UMN 2022–2023 Doctoral Dissertation Fellowship. The authors appreciate the valuable discussions with Prof. Paul Crowell and Dr. William Peria.

[1] J.-P. Wang, S. S. Sapatnekar, C. H. Kim, P. Crowell, S. Koester, S. Datta, K. Roy, A. Raghunathan, X. S. Hu, M. Niemier *et al.*, Invited: A pathway to enable exponential scaling for the beyond-CMOS era, in *Proceedings of the 54th Annual Design*

Automation Conference (2017) (Association for Computing Machinery, Austin, TX, 2017), Article 16.

[2] T. L. Gilbert, A phenomenological theory of damping in ferromagnetic materials, IEEE Trans. Magn. **40**, 3443 (2004).

[3] T. Liu, L. Ma, S. Q. Zhao, D. D. Ma, L. Li, G. Cheng, and G. H. Rao, Crystal structure and magnetic properties of Fe_xPd_{1-x} thin films annealed at 550 °C, J. Mater. Sci.: Mater. Electron. **28**, 3616 (2017).

[4] S. Iihama, A. Sakuma, H. Naganuma, M. Oogane, T. Miyazaki, S. Mizukami, and Y. Ando, Low precessional damping observed for $L1_0$-ordered FePd epitaxial thin films with large perpendicular magnetic anisotropy, Appl. Phys. Lett. **105**, 142403 (2014).

[5] M. Kohda, S. Iimori, R. Ohsugi, H. Naganuma, T. Miyazaki, Y. Ando, and J. Nitta, Structural and magnetic properties of $L1_0$-FePd/MgO films on gaas and InP lattice mismatched substrates, Appl. Phys. Lett. **102**, 102411 (2013).

[6] M. Ohtake, S. Ouchi, F. Kirino, and M. Futamoto, Structure and magnetic properties of CoPt, CoPd, FePt, and FePd alloy thin films formed on MgO(111) substrates, IEEE Trans. Magn. **48**, 3595 (2012).

[7] S. Iihama, A. Sakuma, H. Naganuma, M. Oogane, S. Mizukami, and Y. Ando, Influence of $L1_0$ order parameter on Gilbert damping constants for FePd thin films investigated by means of time-resolved magneto-optical Kerr effect, Phys. Rev. B **94**, 174425 (2016).

[8] Y. Zhang, G. Cheng, X. Xu, and L. Li, Effect of change in thickness of Ag toplayer on the structure and magnetic properties of FePd films grown on glass substrate, J. Wuhan Univ. Technol. **33**, 1082 (2018).

[9] X. Wang, S. Krylyuk, D. Josell, D. Zhang, D. Lyu, J.-P. Wang, and D. B. Gopman, Buffer layer engineering of $L1_0$ FePd thin films with large perpendicular magnetic anisotropy, AIP Adv. **11**, 025106 (2021).

[10] D. Zhang, D. Huang, R. J. Wu, D. Lattery, J. Liu, X. Wang, D. B. Gopman, K. A. Mkhoyan, J.-P. Wang, and X. Wang, Low Gilbert damping and high thermal stability of Ru-seeded $L1_0$-phase FePd perpendicular magnetic thin films at elevated temperatures, Appl. Phys. Lett. **117**, 082405 (2020).

[11] M. Futamoto, M. Nakamura, M. Ohtake, N. Inaba, and T. Shimotsu, Growth of $L1_0$-ordered crystal in FePt and FePd thin films on MgO(001) substrate, AIP Adv. **6**, 085302 (2016).

[12] J. R. Skuza, C. Clavero, K. Yang, B. Wincheski, and R. A. Lukaszew, Microstructural, magnetic anisotropy, and magnetic domain structure correlations in epitaxial FePd thin films with perpendicular magnetic anisotropy, IEEE Trans. Magn. **46**, 1886 (2010).

[13] J. M. Iwata-Harms, G. Jan, H. Liu, S. Serrano-Guisan, J. Zhu, L. Thomas, R. Y. Tong, V. Sundar, and P. K. Wang, High-temperature thermal stability driven by magnetization dilution in CoFeB free layers for spin-transfer-torque magnetic random access memory, Sci. Rep. **8**, 14409 (2018).

[14] R. Urban, G. Woltersdorf, and B. Heinrich, Gilbert Damping in Single and Multilayer Ultrathin Films: Role of Interfaces in Nonlocal Spin Dynamics, Phys. Rev. Lett. **87**, 217204 (2001).

[15] Y. Tserkovnyak, A. Brataas, and G. E. W. Bauer, Enhanced Gilbert Damping in Thin Ferromagnetic Films, Phys. Rev. Lett. **88**, 117601 (2002).

[16] P. He, X. Ma, J. W. Zhang, H. B. Zhao, G. Lüpke, Z. Shi, and S. M. Zhou, Quadratic Scaling of Intrinsic Gilbert Damping with Spin-Orbital Coupling in $L1_0$ FePdPt Films: Experiments and Ab Initio Calculations, Phys. Rev. Lett. **110**, 077203 (2013).

[17] V. Kamberský, On ferromagnetic resonance damping in metals, Czech. J. Phys. B **26**, 1366 (1976).

[18] V. Kamberský, Spin-orbital Gilbert damping in common magnetic metals, Phys. Rev. B **76**, 134416 (2007).

[19] K. Gilmore, Y. U. Idzerda, and M. D. Stiles, Identification of the Dominant Precession-Damping Mechanism in Fe, Co, and Ni by First-Principles Calculations, Phys. Rev. Lett. **99**, 027204 (2007).

[20] K. Gilmore, Y. U. Idzerda, and M. D. Stiles, Spin-orbit precession damping in transition metal ferromagnets, J. Appl. Phys. **103**, 07D303 (2008).

[21] T. Qu and R. H. Victora, Effect of substitutional defects on Kambersky damping in $L1_0$ magnetic materials, Appl. Phys. Lett. **106**, 072404 (2015).

[22] J. E. Gómez, B. Zerai Tedlla, N. R. Álvarez, G. Alejandro, E. Goovaerts, and A. Butera, Spin transport parameters in $Ni_{80}Fe_{20}$/Ru and $Ni_{80}Fe_{20}$/Ta bilayers, Phys. Rev. B **90**, 184401 (2014).

[23] T. G. A. Verhagen, H. N. Tinkey, H. C. Overweg, M. van Son, M. Huber, J. M. van Ruitenbeek, and J. Aarts, Temperature dependence of spin pumping and Gilbert damping in thin Co/Pt bilayers, J. Phys.: Condens. Matter **28**, 056004 (2016).

[24] See Supplemental Material at http://link.aps.org/supplemental/10.1103/PhysRevMaterials.6.113402 for details of sample fabrication, characterization, and data analyses.

[25] D. Huang, D. Lattery, and X. Wang, Materials engineering enabled by time-resolved magneto-optical Kerr effect for spintronic applications, ACS Appl. Electron. Mater. **3**, 119 (2021).

[26] D. M. Lattery, D. Zhang, J. Zhu, X. Hang, J. P. Wang, and X. Wang, Low Gilbert damping constant in perpendicularly magnetized W/CoFeB/MgO films with high thermal stability, Sci. Rep. **8**, 13395 (2018).

[27] H. F. Schaake, Thermal expansion of iridium from 4.2 ° to 300 °K, J. Less-Common Met. **15**, 103 (1968).

[28] A. Al-Ghaferi, P. Müllner, H. Heinrich, G. Kostorz, and J. M. K. Wiezorek, Elastic constants of equiatomic $L1_0$-ordered FePd single crystals, Acta Mater. **54**, 881 (2006).

[29] H. Shima, K. Oikawa, A. Fujita, K. Fukamichi, K. Ishida, and A. Sakuma, Lattice axial ratio and large uniaxial magnetocrystalline anisotropy in $L1_0$-type FePd single crystals prepared under compressive stress, Phys. Rev. B **70**, 224408 (2004).

[30] S. Okamoto, N. Kikuchi, O. Kitakami, T. Miyazaki, Y. Shimada, and K. Fukamichi, Chemical-order-dependent magnetic anisotropy and exchange stiffness constant of FePt (001) epitaxial films, Phys. Rev. B **66**, 024413 (2002).

[31] D. M. Lattery, J. Zhu, D. Zhang, J. P. Wang, P. A. Crowell, and X. Wang, Quantitative analysis and optimization of magnetization precession initiated by ultrafast optical pulses, Appl. Phys. Lett. **113**, 162405 (2018).

[32] J. M. Beaujour, D. Ravelosona, I. Tudosa, E. E. Fullerton, and A. D. Kent, Ferromagnetic resonance linewidth in ultrathin films with perpendicular magnetic anisotropy, Phys. Rev. B **80**, 180415(R) (2009).

[33] J. B. Staunton, L. Szunyogh, A. Buruzs, B. L. Gyorffy, S. Ostanin, and L. Udvardi, Temperature dependence of magnetic

anisotropy: an ab initio approach, Phys. Rev. B **74**, 144411 (2006).

[34] A. Korolev, N. Vlasova, O. Golovina, S. Okatov, J. Barker, B. Greenberg, O. Klementjeva, A. Volkov, and O. N. Mryasov, Temperature dependence of magnetic anisotropy for single domain $L1_0$ FePd crystal and role of the ordering defects, in *2015 IEEE International Magnetics Conference (INTERMAG)* (IEEE, 2015).

[35] H. Shima, K. Oikawa, A. Fujita, K. Fukamichi, and K. Ishida, Magnetic anisotropy and mangnetostriction in $L1_0$ FePd alloy, J. Magn. Magn. Mater. **272-276**, 2173 (2004).

[36] H. B. Callen and E. Callen, The present status of the temperature dependence of magnetocrystalline anisotropy, and the $l(l+1)2$ power law, J. Phys. Chem. Solids **27**, 1271 (1966).

[37] W. Carr, Jr., Temperature dependence of ferromagnetic anisotropy, Phys. Rev. **109**, 1971 (1958).

[38] J. Foros, G. Woltersdorf, B. Heinrich, and A. Brataas, Scattering of spin current injected in Pd(001), J. Appl. Phys. **97**, 10A714 (2005).

[39] J. M. Shaw, H. T. Nembach, and T. J. Silva, Determination of spin pumping as a source of linewidth in sputtered $Co_{90}Fe_{10}$/Pd multilayers by use of broadband ferromagnetic resonance spectroscopy, Phys. Rev. B **85**, 054412 (2012).

[40] S. Yakata, Y. Ando, T. Miyazaki, and S. Mizukami, Temperature dependences of spin-diffusion lengths of Cu and Ru layers, Jpn. J. Appl. Phys. **45**, 3892 (2006).

[41] X. Yang, S. Zhang, Q. Li, G. Zhao, and S. Li, The abnormal damping behavior due to the combination between spin pumping and spin back flow in $Ni_{80}Fe_{20}$/Ru_t bilayers, J. Magn. Magn. Mater. **502**, 166495 (2020).

[42] C. Swindells, A. T. Hindmarch, A. J. Gallant, and D. Atkinson, Spin transport across the interface in ferromagnetic/nonmagnetic systems, Phys. Rev. B **99**, 064406 (2019).

[43] K. Roy, Estimating the spin diffusion length and the spin Hall angle from spin pumping induced inverse spin Hall voltages, Phys. Rev. B **96**, 174432 (2017).

[44] T. Fache, J. C. Rojas-Sanchez, L. Badie, S. Mangin, and S. Petit-Watelot, Determination of spin Hall angle, spin mixing conductance, and spin diffusion length in CoFeB/Ir for spin-orbitronic devices, Phys. Rev. B **102**, 064425 (2020).

[45] A. Cohen, A. Jonville, Z. Liu, C. Garg, P. C. Filippou, and S.-H. Yang, Current driven chiral domain wall motions in synthetic antiferromagnets with Co/Rh/Co, J. Appl. Phys. **128**, 053902 (2020).

[46] S. Panda, S. Mondal, J. Sinha, S. Choudhury, and A. Barman, All-optical detection of interfacial spin transparency from spin pumping in β-Ta/CoFeB thin films, Sci. Adv. **5**, eaav7200 (2019).

[47] A. Ruiz-Calaforra, T. Brächer, V. Lauer, P. Pirro, B. Heinz, M. Geilen, A. V. Chumak, A. Conca, B. Leven, and B. Hillebrands, The role of the non-magnetic material in spin pumping and magnetization dynamics in NiFe and CoFeB multilayer systems, J. Appl. Phys. **117**, 163901 (2015).

[48] C. Du, H. Wang, F. Yang, and P. C. Hammel, Systematic variation of spin-orbit coupling with d-orbital filling: Large inverse spin Hall effect in 3d transition metals, Phys. Rev. B **90**, 140407(R) (2014).

[49] T. White, T. Bailey, M. Pierce, and C. W. Miller, Strong spin pumping in permalloy-iridium heterostructures, IEEE Magn. Lett. **8**, 1 (2017).

[50] O. Mosendz, J. E. Pearson, F. Y. Fradin, G. E. W. Bauer, S. D. Bader, and A. Hoffmann, Quantifying Spin Hall Angles from Spin Pumping: Experiments and Theory, Phys. Rev. Lett. **104**, 046601 (2010).

[51] S. Mizukami, Y. Ando, and T. Miyazaki, Ferromagnetic resonance linewidth for NM/80NiFe/NM films (NM = Cu, Ta, pd and Pt), J. Magn. Magn. Mater. **226-230**, 1640 (2001).

[52] Y. Tserkovnyak, A. Brataas, and G. E. W. Bauer, Spin pumping and magnetization dynamics in metallic multilayers, Phys. Rev. B **66**, 224403 (2002).

[53] F. D. Czeschka, L. Dreher, M. S. Brandt, M. Weiler, M. Althammer, I. M. Imort, G. Reiss, A. Thomas, W. Schoch, W. Limmer *et al.*, Scaling Behavior of the Spin Pumping Effect in Ferromagnet-Platinum Bilayers, Phys. Rev. Lett. **107**, 046601 (2011).

[54] R. Gupta, N. Behera, V. A. Venugopal, S. Basu, A. K. Puri, P. Ström, M. A. Gubbins, L. Bergqvist, R. Brucas, P. Svedlindh *et al.*, Engineering of spin mixing conductance at Ru/FeCo/Ru interfaces: effect of re doping, Phys. Rev. B **101**, 024401 (2020).

[55] V. A. Atsarkin, I. V. Borisenko, V. V. Demidov, and T. A. Shaikhulov, Temperature dependence of pure spin current and spin-mixing conductance in the ferromagnetic—normal metal structure, J. Phys. D: Appl. Phys. **51**, 245002 (2018).

[56] L. Wang, Z. Fan, A. G. Roy, and D. E. Laughlin, Effects of atomic ordering on the curie temperature of FePd $L1_0$ type alloys, J. Appl. Phys. **95**, 7483 (2004).

[57] R. Powell, R. Tye, and J. Woodman Margaret, Thermal conductivities and electrical resistivities of the platinum metals, Platin. Met. Rev. **6**, 138 (1962).